Strong renormalization of Ba vibrations in thermoelectric type IX clathrate Ba24Ge100

Romain Viennois, M. Beaudhuin, M M Koza

Strong renormalization of Ba vibrations in thermoelectric type IX clathrate $Ba_{24}Ge_{100}$

R. Viennois[a,1], M. Beaudhuin[a], M. M. Koza[b]

[a] ICGM, Univ Montpellier, CNRS, ENSCM, Montpellier, France

[b] Institut Laue Langevin, 71 Avenue des Martyrs, CS 20156, F-38042 Grenoble, France.

Abstract

We report a combined experimental and theoretical study of the lattice dynamics of the type IX clathrate $Ba_{24}Ge_{100}$ by inelastic neutron scattering (INS) experiments and Density Functional Theory (DFT) calculations. We observe low-energy optical modes at about 2-3 meV due to the motion of the heavy Ba atoms along the high symmetry axis and the largest dimension of the open Ge@20 cages present in the compound. Even though the phonon participation ratio indicates that these low-energy modes are localized, their Q dependence shows that the dynamics of the Ba guests are correlated. We observe a strong change in the spectral weight of these modes when the compound undergoes a temperature-induced structural transformation in the temperature range 190-230 K. In the high-temperature phase the low-energy optical modes show high intensities in the INS data and frequencies rather insensitive to temperature changes up to about 550 K. In the low-temperature structural modification, the low-energy mode intensities are strongly depleted and apparently shifted to higher energies, this behavior is in line with an off-centering of the Ba atoms at low temperatures. Our DFT calculations successfully approximate the essential features in the dynamics of the high-temperature $Ba_{24}Ge_{100}$ structure.

Keywords: Phonons, Clathrate, Inelastic Neutron Scattering, DFT

[1] Corresponding author: romain.viennois@umontpellier.fr

Introduction

The study of thermoelectric materials is a growing field due to the emergency to find new environment friendly energy sources. The efficiency of thermoelectric materials is represented by the dimensionless Figure of Merit $ZT = S^2\sigma T/\lambda$, with S the Seebeck coefficient, σ the electrical conductivity, λ the thermal conductivity and T the absolute temperature. To reach high efficiencies, thermoelectric materials need to be poor thermal conductors, thus, to exhibit a λ as low as possible[1].

During the last two decades, new thermoelectric materials were found showing advanced efficiencies for high temperature thermoelectric applications. The reduced λ was accomplished by following some simple concepts such as the phonon glass electron crystal (PGEC) idea proposed by G. Slack [2]. Cage compounds such as clathrates and filled skutterudites are two groups of structurally complex compounds to which the PGEC concept was applied with great success [3,4]. However, up to date the origin of the microscopic mechanism behind the low thermal conductivity is disputed, although it is clearly related to the vibrations of the atoms intercalated within the spacious cages of these cage compounds.

In the past, it was proposed that phonon Umklapp scattering was enhanced in filled skutterudites because of additional scattering channels for heat-carrying acoustic phonons introduced by the presence of low-lying optical modes. The low-energy optical modes involve mainly motions of heavy rare-earth atoms intercalated in the spacious cages [5].

Later on, our experimental studies supported this scenario by careful measurements of phonon density of states of filled RFe_4Sb_{12} (R = La, Ce) skutterudites [6] as well as phonon dispersion of $LaFe_4Sb_{12}$ [7] and showed that the low-lying optical modes were strongly harmonic, which contrasts the resonant scattering scenario proposed in the "rattling" picture. We also found similar behavior in the metastable type 1 Ba_8Si_{46} clathrate, which contains two types of cages [8]. However, in some other cage compounds such as osmate pyrochlore [9], RV_2Al_{20} with R =Al, Ga [10] or type VIII $Ba_8Ga_{16}Sn_{30}$ clathrate [11], a large anharmonicity was found for the low-lying optical modes involving mainly motions of the intercalated atoms.

We recently investigated the metastable type IX chiral cubic $Ba_{24}Si_{100}$ clathrate, which contains 3 types of cages and has no equivalent counterpart among hydrate or silicate clathrates. In this structure, 8 Ba1

atoms are located in closed Si@20 cages 4 Ba2 atoms are located in distorted cubic Si@8 cages and 12 Ba3 atoms are located in open Si@20 cages. We found significant anharmonicity for the vibrations of the Ba atoms along the larger dimensions of the large open Si@20 cages with energies as low as 2-3 meV [12]. There exist other type IX clathrates such as $Ba_{24}Ge_{100}$, having the advantage of being thermodynamically stable [13-15]. This compound has very interesting properties such as superconductivity at low temperature, 1st order metal-semiconductor transition which is accompanied by a temperature-induced structural transformation in the 150-250 K temperature range whose origin is still under discussion [13-20]. The low-temperature phase has the same space group as the room-temperature phase but the Ba atoms located in the distorted cubic Ge@8 interstices and in the open Ge@20 cages become locked in at split sites [17-20].

The electronic structures of both room- and low-temperature phases were studied by DFT calculations [21,22] as well as by X-ray photoemission spectroscopy [23,24]. A strong decrease of the density of states at the Fermi level was observed in the low-temperature phase [23,24] and confirmed by nuclear magnetic resonance (NMR) experiments [25,26]. Diffraction studies also indicate an anomalous behavior of the thermal expansion in the region of the structure transformation: the thermal expansion becomes negative in the 190-230 K temperature range [19,20]. These studies also indicate an increase of the anisotropy of the charge density of the Ba atoms intercalated in the open Ge@20 cages during the phase transition pointing to the essential role played by their vibrations during the temperature-induced structure transformation [19,20].

When high pressure is applied on $Ba_{24}Ge_{100}$, the temperature of the metal-semiconductor transition decreases and eventually disappears at 2.8 GPa [16]. In the same time, the superconducting temperature is 16-fold enhanced, mainly by the increase of the density of states at the Fermi level [16,27]. The metal-semiconductor transition temperature also decreases when $Ba_{24}Ge_{100}$ is alloyed with Eu or Na on the Ba site and even disappears when one third of Ba is replaced by Na [16,17]. Interestingly, when the Ge site is substituted by an element of the third column, the structure transformation temperature is lowered. One also notices that the thermal conductivity decreases to ~ 0.8 W/m.K for $Ba_{24}Ga_{15}Ge_{85-x}$ which is a very good thermoelectric material with ZT reaching a value as high as 1.3 at about 680°C [28-30].

The above results call for a thorough investigation of the lattice dynamics of $Ba_{24}Ge_{100}$, especially to understand the role played by the dynamics of the guest atoms in the structural transition observed in the parent compound $Ba_{24}Ge_{100}$ and to comprehend the origin of the low thermal conductivity induced by a substitution on the Ge sites. Although, these compounds have very interesting properties, there are no lattice dynamics (LD) studies at low T carried out, only a Raman study under high pressure (up to 26 GPa) has been reported.[31] Neither inelastic neutron scattering (INS) experiments monitoring the vibrational properties nor ab initio density functional theory (DFT) calculations of the lattice dynamics of these compounds have been reported, yet.

The present work reports on the lattice dynamics of the type IX clathrate $Ba_{24}Ge_{100}$. We first report a combined study of the harmonic properties and lattice dynamics of $Ba_{24}Ge_{100}$ with DFT calculations and spectroscopic tools such as INS experiments. We then report the INS experiments as a function of temperature in order to probe the changes induced by the phase transition in the lattice dynamics as well as the anharmonicity. DFT calculations of the atomic potential of the different guest atoms are carried out to study the guest dynamics and their anharmonicity. High temperature X-ray diffraction experiments are performed for determining the thermal expansion and Grüneisen parameter in the high temperature phase.

Experimental and computational details

Sample synthesis and characterization

Polycrystalline samples of $Ba_{24}Ge_{100}$ were prepared by arc melting of Ba (98.5% lump) and Ge (99.999% lump) and found to be single-phase $Ba_{24}Ge_{100}$ as evidenced by x-ray diffraction experiments. The quality of the samples is documented in Appendix A. The specimens were analyzed after synthesis at room temperature by using a x-ray diffraction apparatus (Philips X'PERT PRO II with Cu $K\alpha_1$ and $K\alpha_2$ radiations). Rietveld refinement with Fullprof software was applied for the structural analysis [32]. We found a lattice parameter a = 14.5566(1) Å (χ^2=10.9, R_{Bragg} = 8.57, R_F = 5.36) in good agreement with prior experimental works. The corresponding fractional atomic positions and isotropic atomic

displacement parameters are reported in Table 1. The high-temperature x-ray diffraction experiments were performed using a x-ray diffraction apparatus (Empyrean with Co $K\alpha_1$ and $K\alpha_2$ radiations) and a heater made of Ta under secondary vacuum. The lattice parameters were determined using pattern matching with Fullprof software [32]. The results are depicted in Figure 11a of Appendix A. In order to determine the characteristic temperatures of the metal-insulator and structural transitions, we have carried out magnetic susceptibility experiments under an external magnetic field of 1 T using a Squid Magnetic Properties Measurements Systems (MPMS) apparatus from Quantum Design. The results are reported in Figure 11b of Appendix A. Our results agree well with those of Paschen et al. [17].

Inelastic neutron scattering experiments

High-resolution INS experiments were performed with the cold-neutron time-of-flight spectrometers IN5 and IN6 at the Institut Laue Langevin in Grenoble, France. The IN5 spectrometer was utilized with the incident wavelengths of 1.8, 2.5 and 5 Å resulting in an elastic energy resolution of 1.5, 0.6 and 0.08 meV, respectively. A wavelength of 4.14 Å with an elastic resolution of 0.17 meV was utilized at the IN6 spectrometer. Basic corrections were applied to the recorded data comprising empty holder scattering, frame overlap and instrument background signals, scaling for different detector efficiencies as well as its energy dependence. The signal was transformed after to the dynamical structure factor applying established mathematical relations. The generalized density of states (GDOS) was computed within the incoherent approximation for coherently scattering materials similarly to a recent approach performed for skutterudites and Ba-Ge clathrates [33-36]. As Ba and Ge atoms are rather weak neutron scatterers, the signal of the sample was low, even with about 7 g of sample material, which makes the determination of the Q dependence of the dynamical structure factor challenging.

Ab initio and lattice dynamics calculations

Lattice dynamics calculations were carried out with the direct method from the Hellmann-Feynman (HF) forces computed on the relaxed clathrate structures with the Vienna Ab-initio Software Package (VASP). The DFT calculation was based on projector augmented wave (PAW) pseudopotentials and the PBE exchange-correlation functional [37,38]. We have used the finite-temperature smearing first order

Methfessel-Paxton method for the band occupancies [39]. For all calculations an energy cut-off of 350 eV, an energy convergence of 10^{-10} eV and a force convergence of 10^{-4} eV/Å were applied with a Monkhorst-Pack [40] k-mesh of 5x5x5. Detailed information about the relaxed atomic positions and displacement parameters is offered in Table 1. The relaxed lattice parameter found is 14.8636 Å and is by about 2 % larger than the experimental values (14.55-14.56 Å) which is typical to the PBE exchange-correlation functional [41]. We have also calculated the variation of the energy as a function of the volume and from fitting with the Vinet equation [42], and found the bulk modulus B = 37.5 GPa and its pressure derivative dB/dP = 4.75. These values are smaller than the experimental values found by Yuan et al [27]: B = 44(2) GPa and dB/dP = 5.8(8). The electronic density of states is reported in the Appendix B and is in very good agreement with the Zerec's calculations [21].

The HF forces were derived by displacing atoms from their equilibrium positions by 0.03 Å along non-equivalent high-symmetry directions. For the equilibrium configuration, the atom positions were relaxed with a force convergence of 10^{-4} eV/Å. The lattice dynamics properties were computed from the HF forces by the diagonalization of the dynamical matrix with the software package Phonon [43]. For a better comparison of the GDOS with the DFT results, the neutron-weighted phonon density of states Z'(E) was calculated using : $Z'(E) = \sum_i \frac{\sigma_i}{M_i} Z_i(E)$, where Z_i(E) are the atom-projected density of states, σ_i are the scattering cross sections and M_i are the atom masses of each atom. For convenience, Z'(E) was broadened by a Gaussian for better comparison with the experimental data.

The atomic displacement parameters (ADPs) were computed in harmonic approximation [44] The participation ratio p(ω) describes the degree of participation of the different atoms to a particular vibrational eigenstate[12,46,47]. It has been extracted from the above calculations using [12, 45,46]:

$$p(\omega) = \left(\sum_{i=1}^{N} \left|\vec{u}_i(\omega_{\vec{q}})\right|^2\right)^2 / N \sum_{i=1}^{N} \left|\vec{u}_i(\omega_{\vec{q}})\right|^4 \qquad (1)$$

Where $\vec{u}_i = \vec{e}_i(\vec{q})/\sqrt{M_i}$ are the atomic amplitudes with the phonon polarization vector $\vec{e}_i(\vec{q})$ and the mass M_i of atom i.

The calculations of the atomic potential as function of the displacements of the Ba guest atoms Δx has been performed in the same conditions as the calculations of the HF forces.

Atom	Wyckoff	x	y	z	U_{iso}	x	y	z	U_{iso}
Ba1	8c	0.1894(2)	x	x	0.007(1)	0.192	x	x	0.0157
Ba2	4b	7/8	x	x	0.023(2)	7/8	x	x	0.0277
Ba3	12d	1/8	0.8102(2)	y+0.25	0.045(2)	1/8	0.8115	y+0.25	0.064
Ge1	8c	0.0287(3)	x	x	0.026(3)	0.0315	x	x	0.026
Ge2	24e	0.2015(3)	0.0426(3)	0.0004(3)	0.013(2)	0.2041	0.0424	0.0017	0.017
Ge3	12d	1/8	0.1700(3)	y+0.25	0.013(2)	1/8	0.1711	y+0.25	0.018
Ge4	24e	0.2395(3)	0.9338(3)	0.8758(3)	0.012(1)	0.2391	0.9331	0.8756	0.018
Ge5	24e	0.4169(3)	0.8526(3)	0.0835(3)	0.009(1)	0.4167	0.8519	0.0851	0.020
Ge6	8c	0.3267(3)	x	x	0.008(3)	0.3256	x	x	0.017

Table 1: Atomic positions and isotropic atomic displacement parameters of $Ba_{24}Ge_{100}$ at room temperature from Rietveld refinement of XRD data (left) and from DFT calculations (right).

Results

The clathrate $Ba_{24}Ge_{100}$ crystallizes in the non-centrosymmetric chiral cubic structure of space group $P4_132$ (number 213) with 124 atoms in the primitive cell. Thus, there are 372 vibrational eigenmodes. Their irreducible representation at the Brillouin zone center is determined by the group theory to

$$\Gamma_{opt} = 14\ A_1 \oplus 17\ A_2 \oplus 31\ E \oplus 47\ T_1 \oplus 45\ T_2 \text{ and } \Gamma_{ac} = T_1$$

where the A, E and T modes are respectively singly, doubly and triply degenerate. Thus, there are 90 different frequencies associated with Raman-active modes of A_1, E and T_2 symmetry, and 47 different frequencies from infrared-active modes of T_1 symmetry. We present in Fig. 1 the vibrational densities of states (DOS) and the full set of Γ point eigenfrequencies computed from DFT calculations. The complete set of Γ point eigenfrequencies and their symmetries are listed in Appendix B. In Fig. 2 we compare the computed neutron-weighted phonon DOS Z'(E) with the GDOS derived from an INS experiment with 5 Å at 300 K.

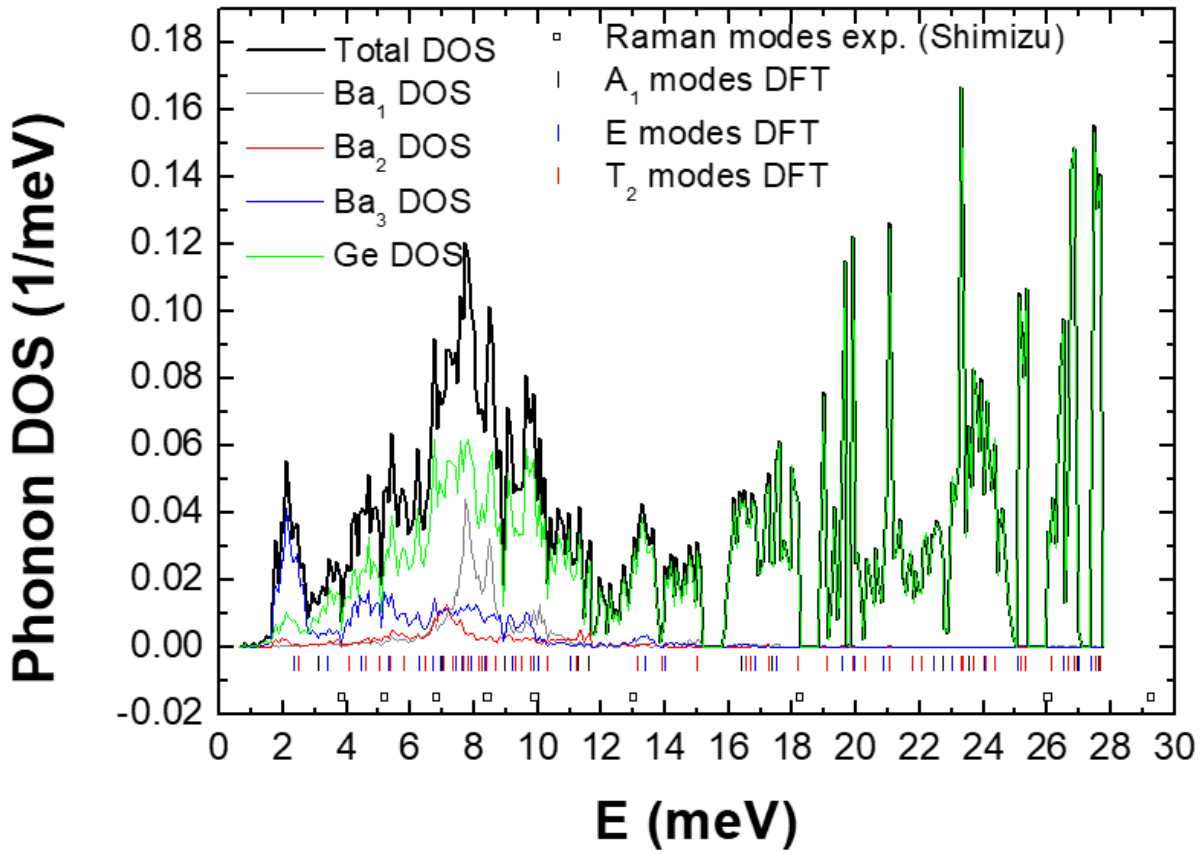

Figure 1: Total and atom-projected DOS of $Ba_{24}Ge_{100}$ obtained from DFT calculations. Contribution from Ba is discriminated according to their Wyckhoff positions. Vertical bars indicate computed Γ point eigen-frequencies, open squares report Raman frequencies measured by Shimizu et al. [31].

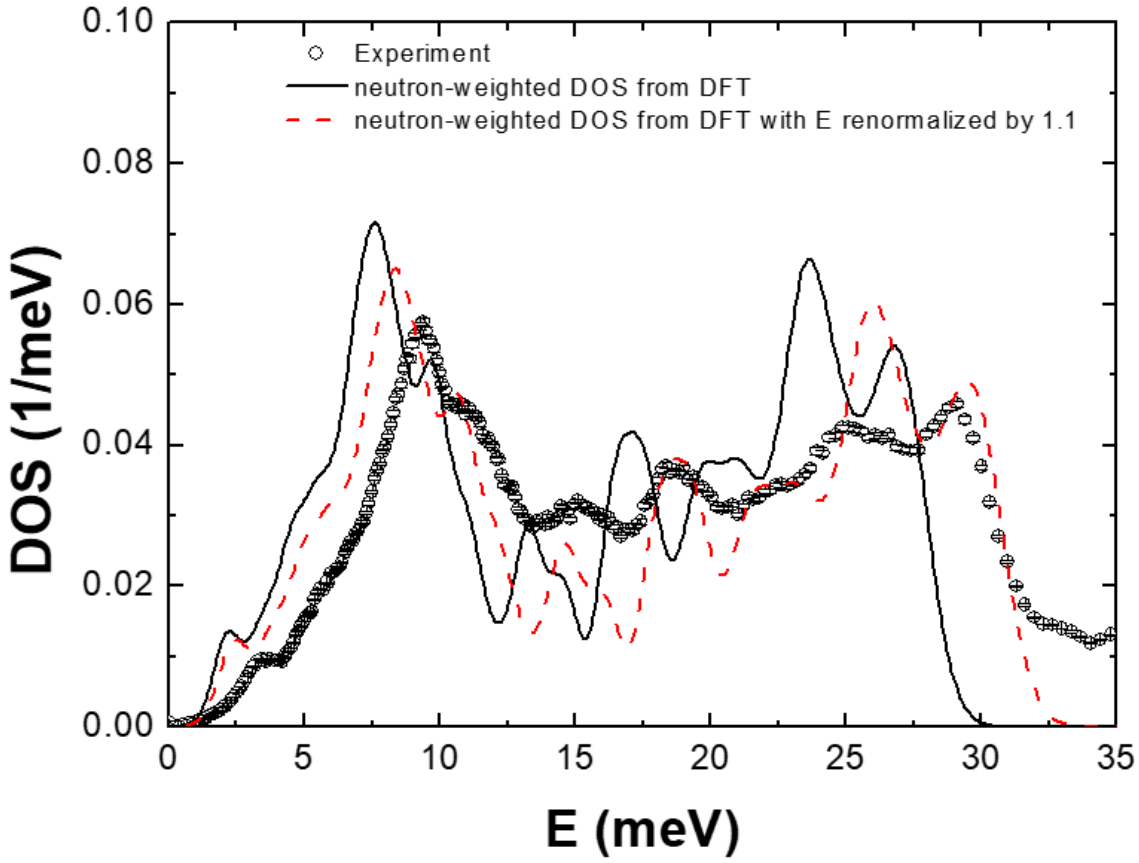

Figure 2: GDOS of $Ba_{24}Ge_{100}$ (empty circles) measured on IN5 at 300 K with 5 Å and neutron-weighted DOS Z'(E) (black solid lines) computed from DFT results and convoluted with a Gaussian mimiking the IN5 energy resolution. Red dashed line corresponds to Z'(E) data with energies renormalized by a factor 1.1 to match the position of the highest energy peak.

As shown in Fig. 2 the measured GDOS of $Ba_{24}Ge_{100}$ extends up to an energy of ~34 meV and is characterized by a strong peak around 10 meV and an overall rich texture indicating localized excitations down to less than 4 meV. A similar behavior has been observed in the two other binary compounds Ba_8Ge_{43} and $BaGe_5$ despite their structural and stoichiometric differences [34,47]. It can be judged from the atom-projected DOS presented in Fig. 1 that the low-energy range of excitations is influenced by Ba amplitudes whereas the high-energy spectral density is dominated by the Ge signal. The details of the atom-projected DOS of the different Ge atoms are given in Appendix B.

Comparing the present data to the dynamics of the isostructural $Ba_{24}Si_{100}$ [8,12] the coupling of Ba to the different host networks becomes obvious by the shift of the dominating low-energy peak from 10 to 20

meV, and the specifics of the host dynamics are highlighted by the shift of the spectral cut-off to more than 52 meV in $Ba_{24}Si_{100}$ [12].

Our lattice dynamics calculations of $Ba_{24}Ge_{100}$ show that the energies of the vibrational modes extend up to about 30 meV. Thus, the DFT calculations underestimate the phonon energies similarly as observed for the cases of Ba_8Ge_{43} [34] and $Ba_{24}Si_{100}$ [12]. This is in line with the overestimation of the lattice parameters by the use of the PBE exchange-correlation functional as we indicate below. However, the neutron-weighted Z'(E) shown in Fig. 2 is capable of reproducing all spectral features identified by the INS experiments. To account for the energy mismatch, we also report Z'(E) with energies renormalized by a factor 1.1. In this case, we observe a good agreement of the different spectral features above 13 meV, thus, for the Ge-dominated vibrations. Nonetheless, there is still disagreement for Ba-influenced excitations below 13 meV and especially for the peak of lowest energy whose characteristic frequency we identify to about 2.2 meV in the DFT calculations and to 3.3 meV in the experiments. Despite the energy mismatch of our calculation all computed features agree well with the experiment data on a qualitative basis.

In a recent extensive DFT work [48], Euchner and Groß addressed and detailed the phonon renormalization problem by different of exchange-correlation functionals for the specific example of type I Ba-Ge clathrates. They have demonstrated that among others comprising PBE the meta-GGA SCAN exchange-correlation functional approximates experimental data best. Such a detailed approach is beyond the scope of our present study.

A congruent conclusion upon underestimation of eigenfrequencies by the PBE functionals can be drawn comparing our DFT data with results from Raman scattering experiments by Shimizu et al [31] both reported in Fig. 1. The experimental Raman spectrum of Shimizu et al [31] extends from 3.85 meV (31 cm^{-1}) to 29.25 meV (236 cm^{-1}) and is upshifted compared to the DFT calculations. Examining the experimental data only, we see that the lowest energy Raman mode at 3.85 meV [31] matches well with the position of the first peak in our INS GDOS data, see Fig. 2. We note that in our DFT data several modes with different symmetries contribute to each of the resolution limited peaks in the INS data. It is therefore impossible to make an unambiguous assignment of specific Raman-active modes to these peaks.

We disclose the low-energy inelastic properties of $Ba_{24}Ge_{100}$ in more detail by reporting in Fig. 3 the DFT-computed phonon dispersion and participation ratios below 12 meV. As evidenced by the phonon dispersion there is a high number of dispersionless, localized phonons contributing to the peak of lowest energy around 2.2 meV. Thus, the intensity of this peak in the DOS is as well formed by vibrational eigenstates away from the Γ point. The localized character of these eigenstates is expressed by their low participation ratio reported on the right hand side of Fig. 3. Similar to the iso-structural $Ba_{24}Si_{100}$ [12] compound the PR takes on numbers as low as 0.037 around the center of the 2.2 meV peak. Another notable point is the position of this peak in comparison to data measured and computed for other Ba-Ge clathrates. We notice that it takes on the lowest value when compared with results of the binary Ba_8Ge_{43} [34], $BaGe_5$ [47], and ternary $Ba_8Ge_{46-x}M_x$ (M=Zn, Pd, Au, Ga) [34,49-52] compounds.

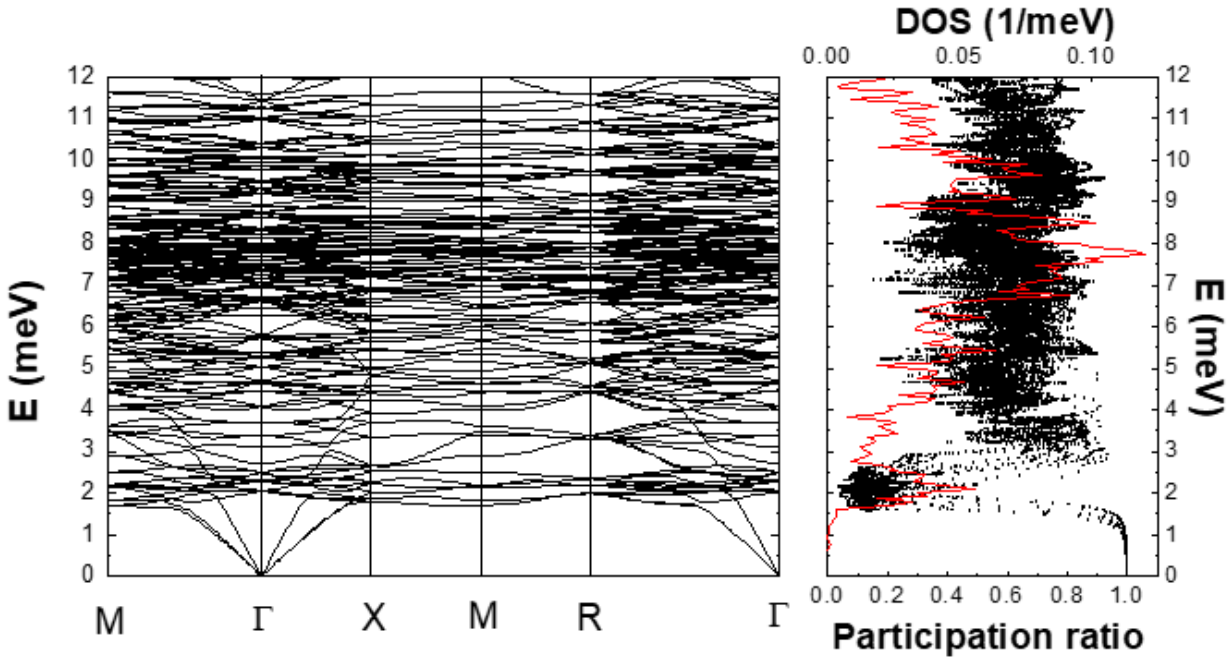

Figure 3: (a) Phonon dispersion and (b) participation ratios of $Ba_{24}Ge_{100}$ based on DFT calculations. For clarity, the corresponding DOS is reported in red with the participation ratio.

The contribution of non-center eigenstates of an energy as low as 2.2 meV manifests itself in a strong dispersionless mode band in the experimental data at 3.3 meV. We demonstrate its existence in Fig. 4 with spectra recorded at IN5 with 2.5 Å incident wavelength and different temperatures. Additional density maps recorded at IN5 with 1.8 Å incident wavelength and different temperatures are plotted in

Appendix C. Above the temperature range of structural transformation (190-230 K) a band of strong intensity centered at around 3.3 meV is observable throughout the entire Q range. In all our high-resolution INS experiments we observe its intensity to be strongest at distinguished Q points of highest Bragg peak intensity and density, i.e. at 2.3 and 3.5 $Å^{-1}$.

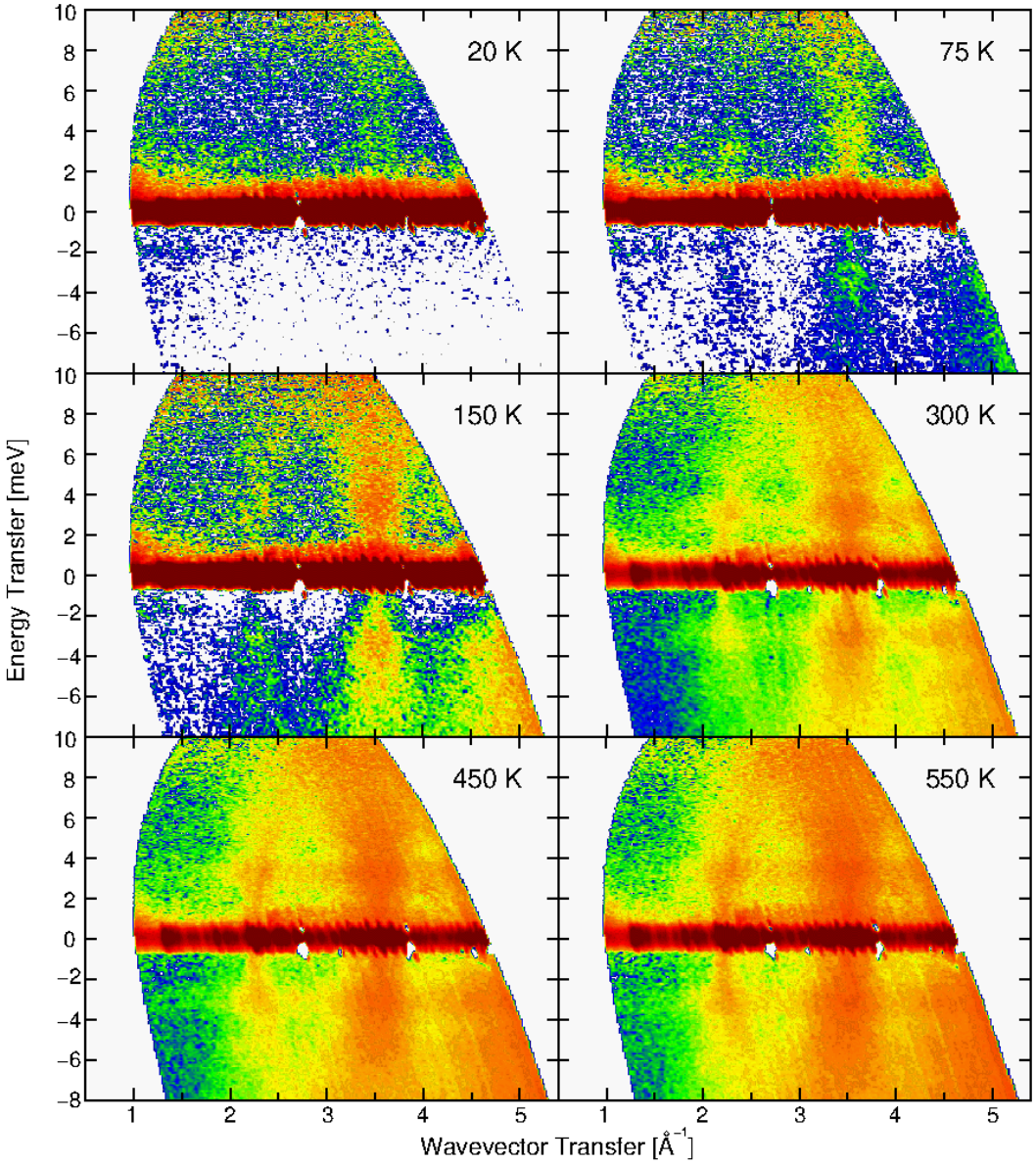

Figure 4: Intensity maps of the dynamic structure factor of $Ba_{24}Ge_{100}$ measured on IN5 with an incident wavelength of 2.5 Å at the indicated temperatures. Note the strong dispersionless excitation band centered at around 3.3 meV formed at T above the structural transformation at 190-230 K.

To shed more light on the underlying modes forming the 2.2 meV peak in the DFT data, we have computed the Ba atomic potentials as a function of the displacements Δx along non-equivalent, high-symmetry directions. The results are plotted in Fig. 5(a). A polynomial function $\Delta E(\Delta x) = K_2\Delta x^2 + K_3\Delta x^3 + K_4\Delta x^4$ was fitted to the data in order to quantify the force constants and the degree of anharmonicity of the Ba vibrations. The harmonic K_2, and anharmonic cubic K_3 and quartic K_4 terms are reported in Table 2. The anharmonicity of the atomic potentials will be discussed latter.

Guest atom	K_2 (eV/Å^2)	K_3 (eV/Å^3)	K_4 (eV/Å^4)	E_2 (meV)	β
Ba_1 (8c)	1.37	0.23	0.75	6.5	0.010
Ba_2 (4b)	1.14		0.87	5.9	0.016
Ba_3 [100] (12d)	0.2	0.00	0.09	2.5	0.023
Ba_3 [001] (12d)	1.04	-0.26	0.89	5.6	0.018

Table 2: Characteristic energies and potential parameters of Ba guests in $Ba_{24}Ge_{100}$ derived from DFT results. K_2, K_3, and K_4 are the harmonic and anharmonic parameters from fitting the potentials with the polynomial function $y = K_2\Delta x^2 + K_3\Delta x^3 + K_4\Delta x^4$. E_2 corresponds to the characteristic energies calculated from K_2, and the dimensionless anharmonic parameter β is computed from the quartic force constant K_4 according to the Dahm-Ueda model[58].

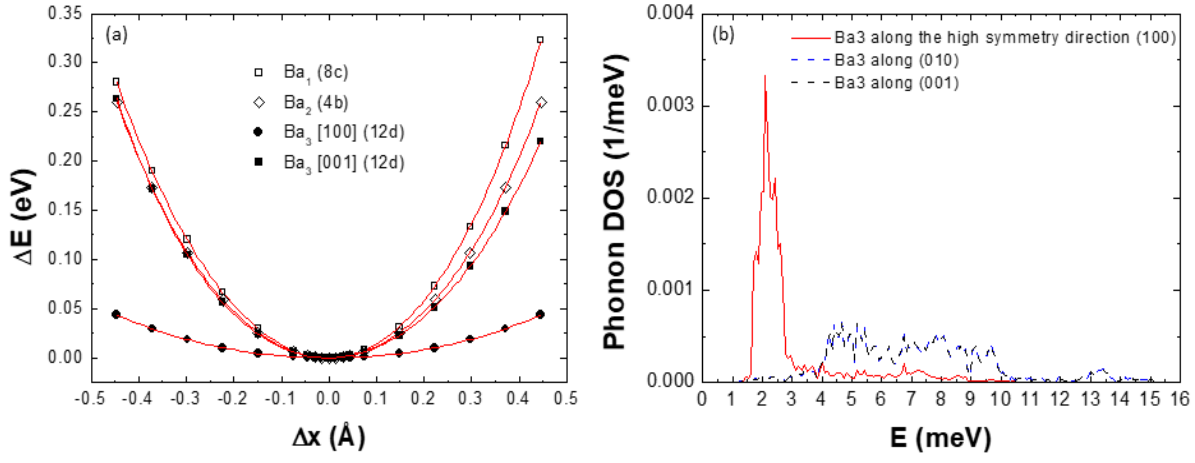

Figure 5: (a) DFT calculated atomic potentials ΔE vs Δx displacement of the Ba atoms in $Ba_{24}Ge_{100}$. The red solid lines represent results from a polynomial fit of fourth order. (b) Directional atom-projected phonon densities of states of the Ba3 atom of $Ba_{24}Ge_{100}$ obtained from DFT calculations.

Any sampled potential energy takes on a minimum at Δx=0, thus, the equilibrium positions of any Ba are at the center of the cages. The harmonic force constants of Ba1, Ba2 and Ba3 along [010]/[001] are rather similar. The decreasing values of K_2 in the sequence of Ba1, Ba2, and Ba3 potentials underline the behavior of the corresponding partial DOS to be located at progressively lower energies shown in Fig. 1. The striking result is the strong depletion of the Ba3 potential along [100]. The associated force constant is smaller than a factor of 5 in comparison to the other values. Consequently, the low-energy peak at 2.2 meV is dominated by the vibrations of Ba3 atoms on (12d) sites with elongations along the largest dimension of the Ge@20 cages, i.e. [100]. We corroborate this statement by presenting the directional partial DOS of the Ba3 atoms on the right hand side of Fig. 5(b).

Similar results have been obtained for Ba3 atoms in $Ba_{24}Si_{100}$[12]. However, in the germanide case the harmonic K_2 of Ba1 and Ba3 along the high symmetry directions are almost two times smaller than in the silicide counterpart. This signifies softer bonding and smaller guest vibrational energies in $Ba_{24}Ge_{100}$ as pointed out above. When compared to Ba_8Ge_{43} we find here smaller K_2 of the guest atoms of up to a factor of 2 for Ba3 along the high symmetry direction[34]. This explains the guest lowest energy among the studied Si- and Ge-based clathrates.

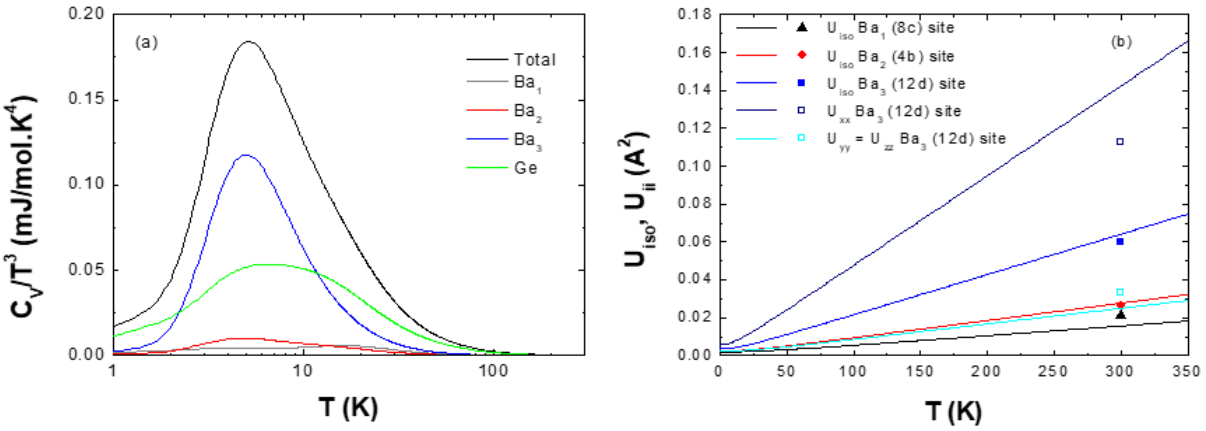

Figure 6: (a) Debye plot of the total and partial heat capacity as a function of temperature. (b) Atomic displacement parameters of barium atoms in $Ba_{24}Ge_{100}$ from DFT calculations compared to experimental results of Fukuoka et al[11].

The presence of low-energy Ba-weighted modes are perceivable in other phonon related observables such as specific heat and atomic displacement parameters. In Fig. 6(a), we report the Debye plot of the heat capacity (C_v/T^3 vs T) of $Ba_{24}Ge_{100}$ obtained from the DFT calculations. We observe a maximum at about 5 K caused by the deviation from the Debye model due to the modes at 2-3 meV. This corroborates the observation done for $Ba_{24}Si_{100}$ where a peak at the higher temperature of 8 K[12] is associated with a larger and anisotropic Debye-Waller factor of the Ba3 atoms, a fingerprint of low-energy optical modes. The notable contribution from the Ge atoms corroborates once more the noteworthy coupling between the Ba guests and the host network. Note that the computation of the C_v/T^3 properties with the high-temperature structure makes a comparison with experimental data as reported by Paschen et al. in reference 17 impractical.

In Fig. 6(b), we compare the anisotropic U_{ii} and isotropic ADPs U_{iso} of the Ba atoms in $Ba_{24}Ge_{100}$ with experimental data. The computed values at 300 K are as well indicated in Tables 1 and 4. The isotropic ADPs U_{iso} of the Ge atoms are reported in Appendix B. Because of the site symmetry, the ADPs of Ba1 and Ba2 atoms are isotropic and we only report their U_{iso}. The largest values of the U_{ii} of the Ba3 atoms are along the high symmetry direction and for the largest dimension of the open Ge@20 cage, here for U_{xx}. As outlined above it is the consequence of the low-energy Ba3 modes in this direction. The comparison with experimental results by Fukuoka[13] reveals a rather good agreement. This is also the case for other experiments reporting ADPs [14,15,53]. Similarly anisotropic and large U_{ii} have been reported for other type IX clathrates and notably large ADPs of guest atoms in the high symmetry direction of the M@20 open cages (M = Si, Ge, Sn) have been observed for all compounds with type IX clathrate structure due to the asymmetric shape of these cages [13-15,28-30,54-56].

The examination of the atom projected DOS (Fig. 1) suggests a much stronger correlation of Ba with Ge atoms in $Ba_{24}Ge_{100}$ than of Ba with Si in $Ba_{24}Si_{100}$[12]. This can be seen in the notable contribution of the lighter Ge atoms to the lowest energy modes at 2-3 meV as well as the participation of the heavy Ba atoms to higher energy vibrations. In $Ba_{24}Si_{100}$ those effects are less prominent. We highlight as well the significant contribution of Ba1 atoms to the peak at about 7-8 meV as well as the participation of Ba3 to the peak around 13 meV dominated by Ge3 and Ge5 atoms. Above 16 meV the signal from Ba is

rather depleted in the phonon DOS and the dynamics is ruled by Ge atoms with alternating contributions from the different sites.

We discuss next the effect of temperature and the temperature-induced structure transformation on the vibrational dynamics. Temperature dependent GDOS data derived from INS experiments at different conditions with the spectrometers IN5 and IN6 are presented in Fig. 7 and Fig. 8(a). Energies of characteristic peaks found in the GDOS data are listed in Table 3. When crossing the region of the structural transition towards low T, one can clearly see: i) a depletion of intensity of the peak at about 3.3 meV [Fig. 7(b) and (d)], ii) a strong upshift of the peak at about 10 meV [Figs. 7(a), 7(c) and 8(a)], iii) a concomitant disappearance of the shoulder at about 11-12 meV, and iv) a strong upshift of the peak at about 19 meV [Fig. 7(a)]. Compared to these strong spectral modifications the GDOS changes very little above the temperature region of structure transformation (190-230 K). As expected from a moderately anharmonic compound, an overall weak softening of phonons up to 550 K is observed. The low-energy peak dominated by the Ba3 dynamics, however, appears rather insensitive to this temperature-induced volume expansion. This indicates a smaller anharmonicity of Ba3 in $Ba_{24}Ge_{100}$ than in $Ba_{24}Si_{100}$ [12]. Note that the opposite behavior is observed in type 1 clathrates, where Ba_8Si_{46} is found less anharmonic than the ternary type 1 Ba-Ga-Ge and Ba-Zn-Ge[8,35,52] compounds. Similar weak anharmonicity of the low-energy optic modes was observed in Ba_8Ge_{43}[35].

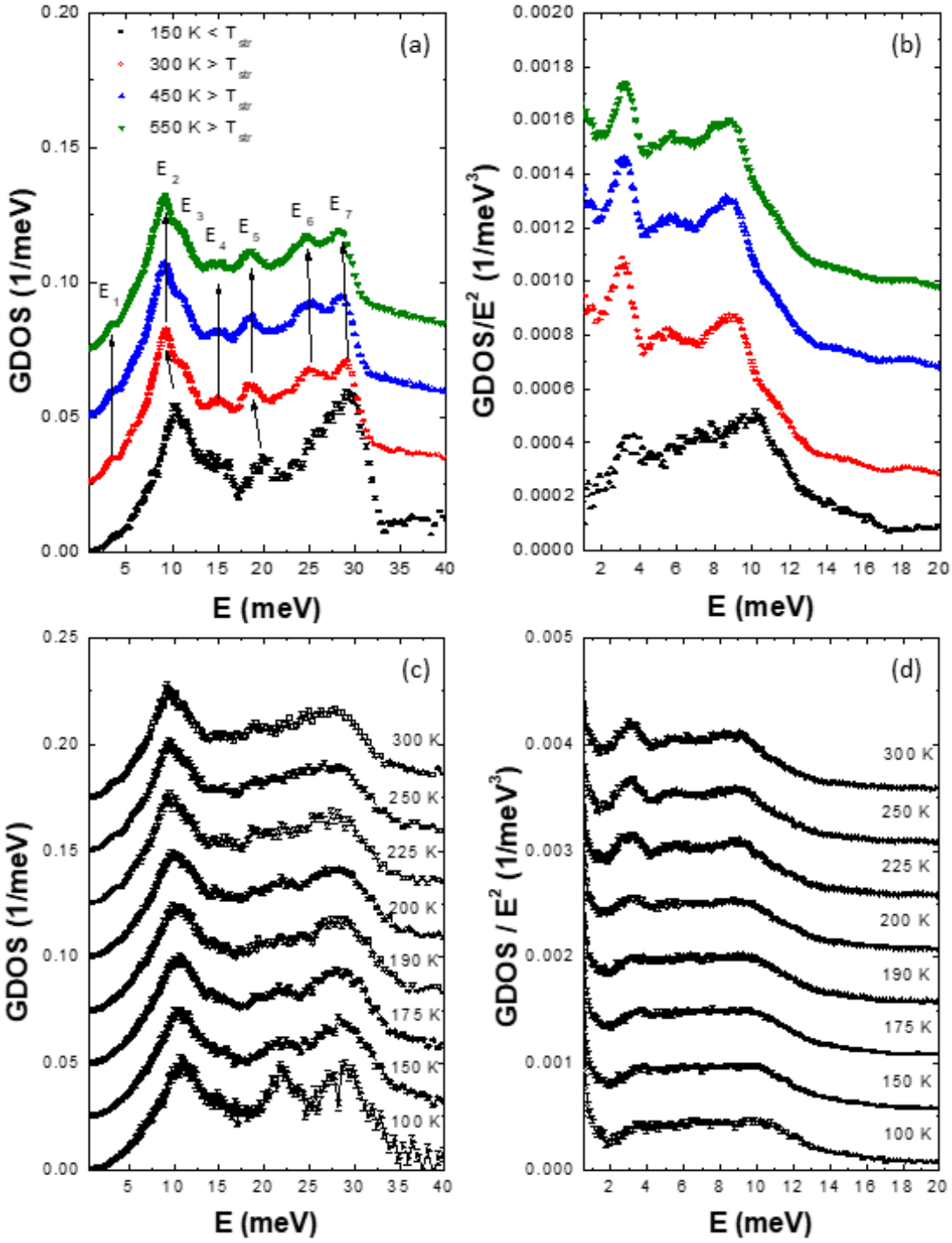

Figure 7: (a) GDOS of $Ba_{24}Ge_{100}$ as a function of temperature derived from INS experiments at IN5 with the incident wavelength of 5 Å. (b) same data sets in a Debye plot GDOS/E^2 vs E. (c) GDOS from INS measurements at IN6 with an incident wavelength of 4.14 Å. (d) same data sets in a Debye plot GDOS/E^2 vs E

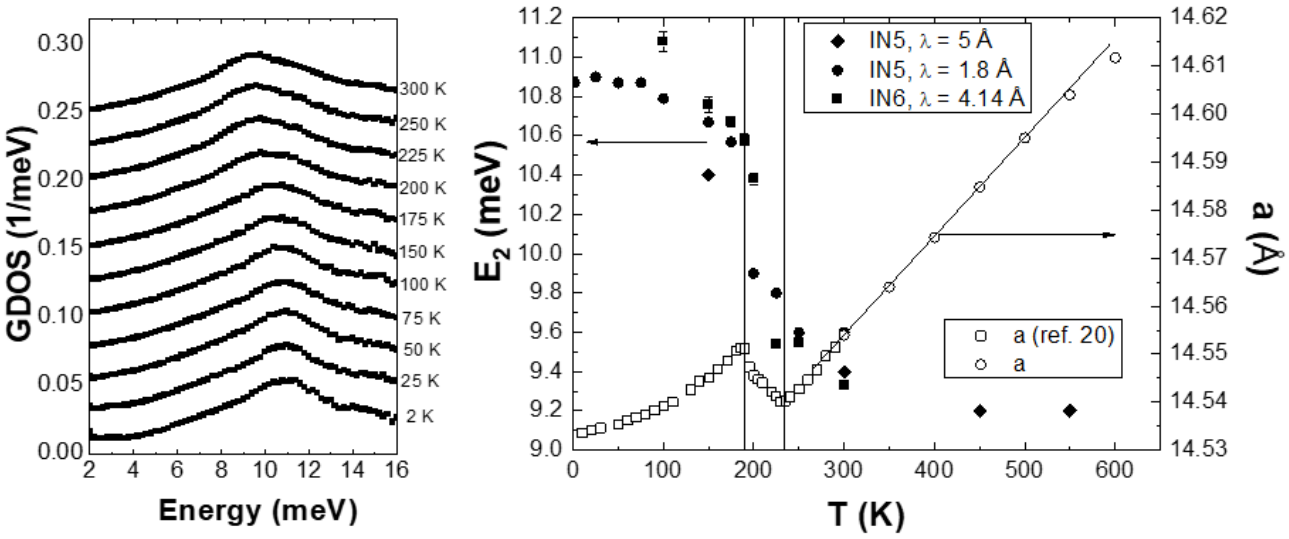

Figure 8: (a) GDOS of $Ba_{24}Ge_{100}$ as function of temperature derived from IN5 data recorded with the incident wavelength of 1.8 Å. (b) Variation of the strong peak at 10 meV as a function of temperature identified in all our INS experiments as well as temperature dependence of the lattice parameter of $Ba_{24}Ge_{100}$ at low (ref. 20) and high temperature (our data) upon heating.

On the contrary, strong spectral modifications of the GDOS occur in the low-energy range of Ba dominated vibrations between 230 K and 190 K, i.e. when cooling through the phase transformation region. Equally, a progressive tapering of the dominating peaks around 22 and 30 meV indicates a spectral modification of the Ge-dominated excitations.

T (K)	E_1 (meV)	E_2 (meV)	E_3 (meV)	E_4 (meV)	E_5 (meV)	E_6 (meV)	E_7 (meV)
150	3.8	10.4			20.1		29.5
300	3.3	9.4	10.8	15.2	18.9	25.2	29.3
450	3.3	9.2	10.8	15.2	18.8	25.5	28.8
550	3.3	9.2	10.5	15	18.77	24.8	28.6

Table 3: Temperature variation of peak energies of $Ba_{24}Ge_{100}$ obtained from GDOS data derived from an IN5 experiment with 5 Å incident neutron wavelength. Corresponding peaks are indicated in Fig. 7(a).

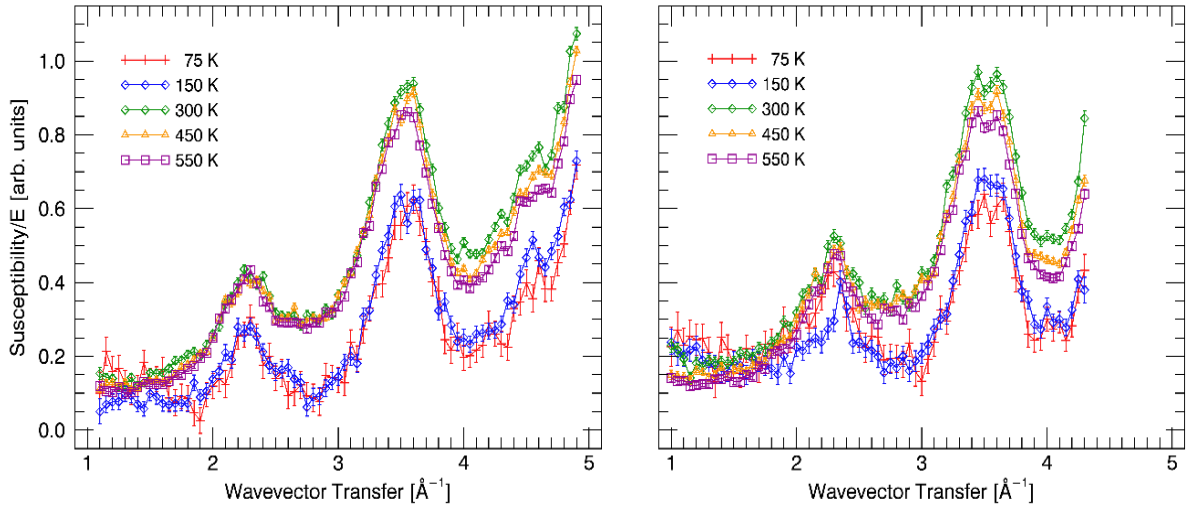

Figure 9: Constant energy cuts through the dynamic susceptibility divided by the energy for 3.5 ± 0.5 meV from IN5 experiments with λ = 2.5 Å. Left, anti-Stokes line and right, Stokes line. 20 K data not shown due to enhanced background contribution. Wavevector transfers with peaking signal (2.3 and 3.5 Å^{-1}) correspond to points with strong Bragg peak intensities and densities the origin of acoustic phonon signal. Note the overall sudden reduction of signal below the temperature of structural transition.

A rather intriguing behavior is detected for the vibrational modes forming the peak at about 3.3 meV in the GDOS as it is documented in Fig. 4. Above the structural transition a localized mode band visible at any Q point of the powder spectra is observed. The powder-averaged form factor indicates that the intensity is however particularly strong at points of strong signals from acoustic phonons.

To elaborate this observation we present cuts through the inelastic response at constant energy and wavevector transfers in Figs. 9 and 10, and Fig. 16 in Appendix C. The plotted signal is the temperature corrected susceptibility divided by the energy transfer for better visibility of the low-energy signal. From the carried out cuts it is obvious to conclude that Brillouin zone center excitations contribute to this vibrational band with prominent eigenvectors as the intensity is most prominent in Q regimes of acoustic phonons emanating from strong Bragg reflections, i.e. Brillouin zone centers.

This conclusion holds as well for temperatures below the structural transition. However, the peak intensity is diminished in comparison to the signal from acoustic phonons. It appears thus more concentrated around Q points of high Bragg peak intensity and density in the powder signal.

As evidenced in Fig. 10(a), the low energy peak is just detectable at the Q points of acoustic signal, it is narrower than above the phase transition [Fig. 10(b)] and, most importantly, it seems to be shifted to higher energies by about 0.5 meV. Fig. 16 of Appendix C highlights this behavior for higher Q points with lower energy resolution.

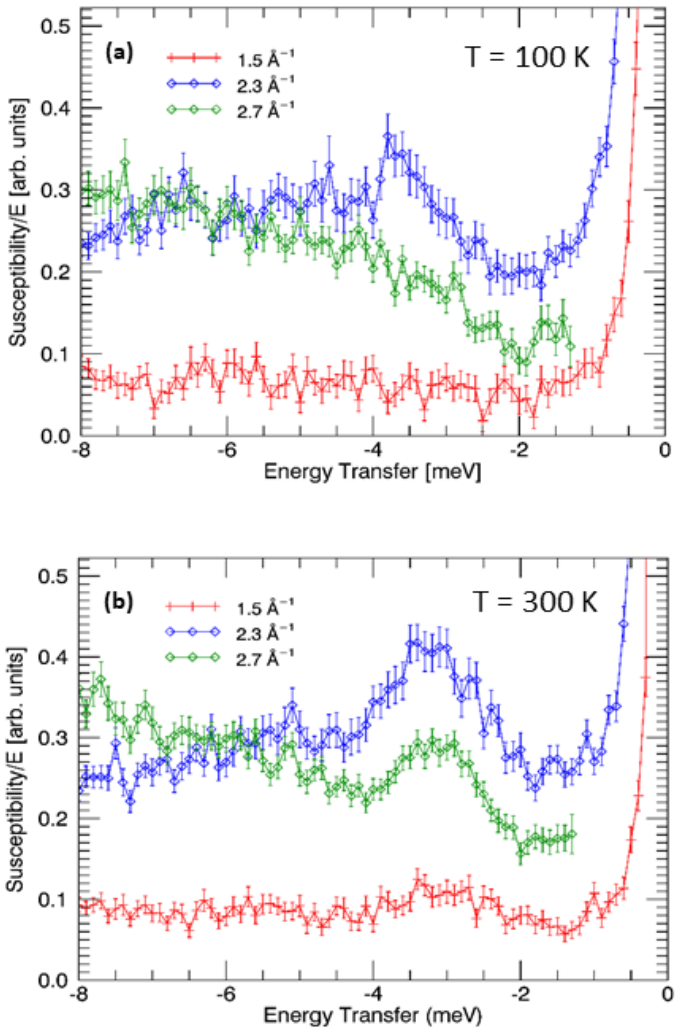

Figure 10: Constant wavevector cuts through the dynamic susceptibility divided by the energy from IN6 experiments with λ = 4.14 Å at 100 K (a) and 300 K (b). Only anti-Stokes line intensity is shown. Note that at 300 K the well defined low-energy peak around 3 meV persists at Q points away from high Bragg peak intensity around 2.3 $Å^{-1}$. This feature is not detectable in the inelastic response below the structural phase transition at 100 K.

To demonstrate the correlation of the changes in the inelastic response of $Ba_{24}Ge_{100}$ with the structural transition we compile in Fig. 8(b) the location of the dominating peak around 10 meV from all our T-dependent INS measurements. For comparison we report the lattice parameter measured by Carillo-Cabrera *et al* [20] from base to room temperature, i.e. crossing the phase transition, and our experimental data expanding the T range up to 600 K. Clearly, in any of the INS data sets the changes in the peak position occur when the temperature-induced structure transformation takes place. Note that the peak downshifts within only 40 K by about 10 % upon heating. In the two temperature domains of structural stability, namely below 190 K and above 230 K, the peak energy changes only moderately by about 2 % within several hundred K. As the behavior in the high T modification is concerned, the low anharmonicity is in line with our DFT data discussed above. We recall that the computed potentials shown in Fig. 5(a) exclude off-centering of any of the Ba positions in the high temperature phase.

As shown in Fig. 1, the vibrations in this energy range are strongly reminiscent of the dynamics of Ba1, Ba2 and Ge. Thus, with the temperature response of the low-energy peak being dominated by the Ba3 dynamics we conclude that the structural variation taking place in the temperature range 190-230 K takes strong influence on the inelastic response of all three Ba sites concomitantly. The enhancement of their characteristic frequencies gives evidence of a stronger bonding and higher correlation with the dynamics of Ge below the transition.

To quantify the anharmonicity of the DFT calculated structure, i.e. the high T phase, and set it in relation to literature data we use the simple model of the anharmonic, isolated oscillator, derived by Dahm and Ueda (DUM) [57]. In this approach, the renormalization of the eigen-energy of a harmonic oscillator, $E_0(T)$, derived as

$$\left(\frac{E_0(T)}{E_0(T=0)}\right)^2 = 1 + \beta\frac{E_0(T)}{E_0(T=0)}\left[\frac{1}{e^{E0(T)/k_BT}-1} + \frac{1}{2} - \frac{1}{2}\frac{E_0(T)}{E_0(T=0)}\right]$$

is given by the anharmonic quartic term K_4 whose amplitude is expressed by the dimensionless parameter $\beta = 4K_4\hbar^4/E_0(T=0)^3M^2$ [57]. Both K_4 and β of the different Ba atoms of $Ba_{24}Ge_{100}$ are calculated from the fit of the atomic potential with a polynomial function in Fig. 5(a) and listed in Table 2. These values are moderate but not negligible, especially for the vibrations of Ba3 along [100]. They are slightly

larger in $Ba_{24}Ge_{100}$ than in $Ba_{24}Si_{100}$ which is a surprising result at a first glance as we have observed a softening of the lowest energy optical modes in $Ba_{24}Si_{100}$ upon cooling[12] which is missing in $Ba_{24}Ge_{100}$.

There are two contributions in the thermal variation of the phonon energies dE/dT [58,59]. On one hand there is the implicit quasi-harmonic contribution due to the volume change $dE_{impl}/dT = -\alpha_V\gamma E(T\rightarrow 0\ K)$ with α_V being the volume thermal expansion, γ being the mode Grüneisen parameter, and on the other, the explicit anharmonic contribution due to the thermal population of the vibrational levels dE_{expl}/dT. If α_V and γ are positive, dE_{impl}/dT would be negative and could compensate the positive dE_{expl}/dT, when β is positive, to explain the absence of temperature dependence of the lowest energy optical modes in $Ba_{24}Ge_{100}$. With these conditions we conjecture that $\alpha_V\gamma$ should be larger in $Ba_{24}Ge_{100}$ than in $Ba_{24}Si_{100}$ because β is larger and hence dE_{expl}/dT in $Ba_{24}Ge_{100}$ than in $Ba_{24}Si_{100}$ [12].

From linear fitting of the lattice parameter between 300 K and 500 K (see Fig. 8(b) for data), we determine the linear thermal expansion $\alpha = \alpha_V/3 = 14.13\ MK^{-1}$ of $Ba_{24}Ge_{100}$. This value is slightly larger than for Ba_8Ge_{43} ($\alpha = 12.65\ MK^{-1}$), $Ba_8Zn_xGe_{46-x}$ ($\alpha = 11.3$ to $13\ MK^{-1}$) and larger or similar than for $Ba_8Ga_{16}Ge_{30}$ ($\alpha = 10$ to $14.2\ MK^{-1}$) [60] as well as larger than for $Ba_{24}Si_{100}$ ($\alpha = 10.6\ MK^{-1}$) and Ba_8Si_{46} ($\alpha = 12.25\ MK^{-1}$)[8]. For the silicides, the thermal expansion is smaller in the type I than in the type IX clathrates in contrast to the germanide clathrates.

From data of pressure-dependent Raman spectroscopy on $Ba_{24}Ge_{100}$ [31] and measured bulk modulus (B = 44 GPa) [27], we determine the rather low Grüneisen parameter $\gamma = 0.9$ for the Raman line at 31.5 cm^{-1} (4 meV). Further we calculate $dE_{impl}/dT = -0.0012\ cm^{-1}/K$ (i. e. -0.15 µeV/K) which results in a decrease of the energy by about 0.04 meV between 300 K and 550 K. This value is too small to be seen in the INS experiments. Note that it is as well about one order of magnitude smaller than the energy variation expected from the explicit contribution determined from the DFT calculations. This means that dE_{expl}/dT and hence β of $Ba_{24}Ge_{100}$ are greatly overestimated by our DFT calculations. This contrasts with the case of $Ba_{24}Si_{100}$ for which β obtained from the DFT calculations was in reasonable agreement with that obtained from the experiments [12].

With the knowledge of the volume thermal expansion α_V, the molar volume V_m, the molar heat capacity C_P [17] and the bulk modulus B [27] of $Ba_{24}Ge_{100}$ at 300 K we compute the thermodynamic Grüneisen parameter $\Gamma = \alpha_V B V_m / C_P$ to 1.12. This is a lower value compared to those of $Ba_{24}Si_{100}$ (Γ = 1.78) and Ba_8Si_{46} (Γ = 1.88) that have been calculated from the data of Lortz et al [8], Toulemonde et al [61] and San Miguel et al [62]. This difference is mainly due to the smaller bulk modulus of $Ba_{24}Ge_{100}$ compared to Ba-Si clathrates.

Conclusion

We have reported for the first time a combined experimental and theoretical study of the lattice dynamics of the type IX clathrate $Ba_{24}Ge_{100}$. There is a good qualitative agreement between the GDOS obtained by the INS experiments and the DOS obtained by the DFT calculations. The experimental ADPs from the literature are well reproduced qualitatively by the DFT calculations. The origin of the low-energy Raman-active modes are obtained thanks to the DFT calculations. The peak at about 3 meV in the GDOS from the INS experiment is due to the low energy optical modes stemming from the motions of the Ba3 guest atom along the high symmetry direction and the largest dimensions of the open Ge_{20} cages. We find that the peak's characteristic energy has no temperature dependence in the high temperature phase and its intensity is strongly depleted as well as apparently shifted to higher energies across the phase transition at low temperature. The absence of temperature dependence of the peak at 3.3 meV in the high temperature phase could be due to a compensation of a softening effect due to the 4^{th} order anharmonicity by the volume contraction upon cooling. We also observed a large change in the spectral weight when the phase transition takes place and especially a large shift of the peak at about 10 meV. We find that $Ba_{24}Ge_{100}$ has a moderate thermodynamic Grüneisen parameter being significantly smaller than those of $Ba_{24}Si_{100}$ and Ba_8Si_{46}.

Acknowledgement

We acknowledge the Institut Laue Langevin for providing beamtime.

Appendix A: Sample characterization

The polycrystalline sample is single-phase as shown by the refinement with the LeBail method of the X-ray diffraction (XRD) data at 300 K with very good refinement quality factors in the Fig.11-(a). The XRD patterns have been measured at high temperatures with Co Kα source. The peaks at about 45°, 83° and 100° are due to the Ta heating plate and are not taken into account in the LeBail refinement. The lattice parameters at high temperature have been obtained by refinement using the LeBail method.

In order to follow the structural transition and determine their transition temperatures T_{s1} and T_{s2} in our sample, we report the magnetic susceptibility with cooling and heating profiles in the Fig. 11-(b), as it has been done by the Dresdner group [16,17]. Our results agree well with these works [16,17].

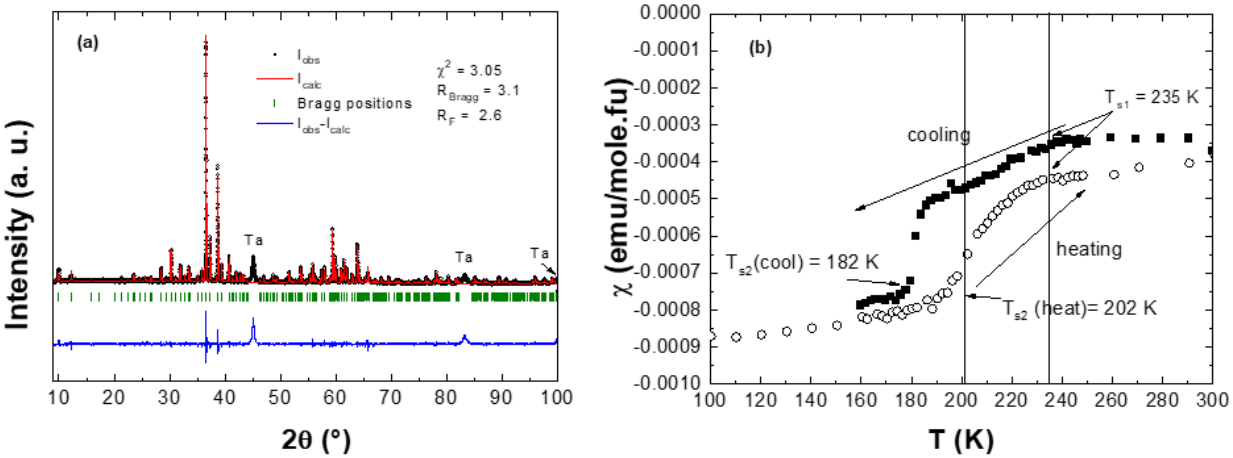

Figure 11: (a) LeBail refinement of the XRD pattern of $Ba_{24}Ge_{100}$ at 300 K. (b) Thermal variation of the magnetic susceptibility of $Ba_{24}Ge_{100}$.

Appendix B: Complementary DFT results

We present here additional useful results from DFT calculations.

The electronic density of states in the Figure 12 is in very good agreement with the Zerec's calculations [21]. We report in the Tables 6 to 8 the frequencies and the symmetries of the different optical modes of $Ba_{24}Ge_{100}$ at Γ point from DFT calculations. We report in the Figure 13 in the atom-projected DOS of the different Ge atoms in $Ba_{24}Ge_{100}$ from DFT calculations. We report in the Figure 14 in the isotropic

ADPs U_{iso} of the different Ge atoms in $Ba_{24}Ge_{100}$ from DFT calculations and compare them with experimental results from Fukuoka et al [13].

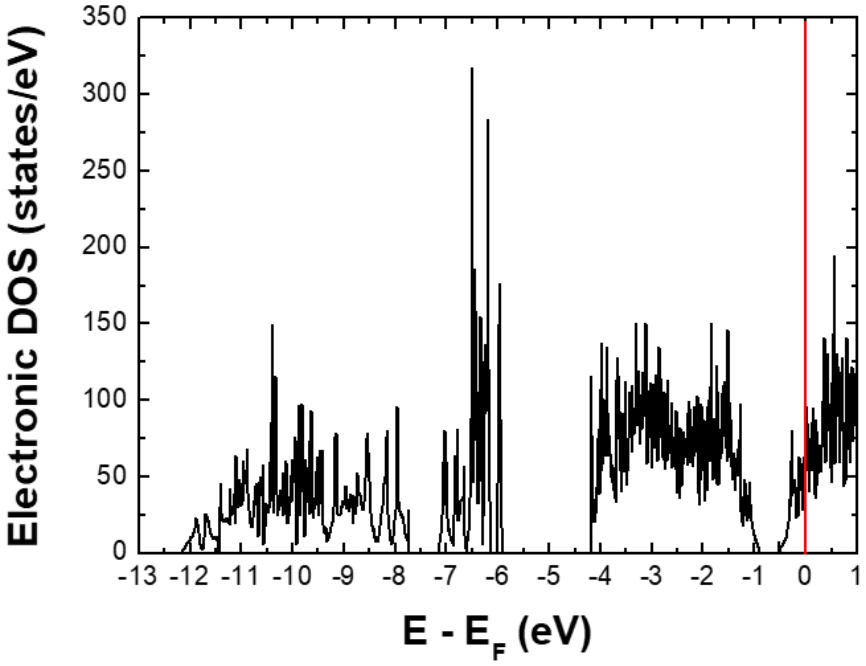

Figure 12: Electronic density of states of $Ba_{24}Ge_{100}$ from DFT calculations.

Atoms	Wyckoff	U_{11} (Å^2)	U_{22} (Å^2)	U_{33} (Å^2)	U_{12} (Å^2)	U_{13} (Å^2)	U_{23} (Å^2)
Ba1	8c	0.0157	U_{11}	U_{11}	0.0006	U_{12}	U_{12}
Ba2	4b	0.0277	U_{11}	U_{11}	0.0084	U_{12}	U_{12}
Ba3	12d	0.1424	0.025	U_{22}	0.0065	-0.0066	0.0061
Ge1	8c	0.0264	U_{11}	U_{11}	0.0039	U_{12}	U_{12}
Ge2	24e	0.0182	0.0162	0.0152	0.0012	0.0028	-0.0022
Ge3	12d	0.0208	0.0159	U_{22}	-0.0021	0.0021	0.0046
Ge4	24e	0.0189	0.0178	0.0157	0.0002	0.001	-0.0047
Ge5	24e	0.0274	0.0167	0.0145	-0.0032	0.0005	0.0013
Ge6	8c	0.0173	U_{11}	U_{11}	-0.0034	U_{12}	U_{12}

Table 4: Anisotropic atomic displacement parameters of $Ba_{24}Ge_{100}$ at 300 K from DFT calculations.

Raman modes	Calculated frequency modes (in cm^{-1})
A_1 symmetry	24.9 ; 56.3 ; 61.4 ; 72.1 ; 90.8 ; 93.6 ; 132 ; 139.9 ; 169.6 ; 183.4 ; 190.1 ; 202.1 ; 217.4 ; 222.6
E symmetry	18.8 ; 27.2 ; 35.8 ; 42.7 ; 50.4 ; 54.2 ; 55.8 ; 60.1 ; 61.3 ; 63.7 ; 67.3 ; 74.1 ; 79.5 ; 80.9 ; 88.9 ; 107.8 ; 112.9 ; 135.5 ; 141.1 ; 157.8 ; 160.9 ; 168.3 ; 181.1 ; 185.6 ; 188.3 ; 193.6 ; 194 ; 202.2 ; 213.7 ; 217.8 ; 220.9
T_2 symmetry	20.1 ; 32.9 ; 37.2 ; 40.6 ; 43.2 ; 46.7 ; 52 ; 56.8 ; 59.3 ; 62 ; 62.9 ; 65.6 ; 66.4 ; 67.5 ; 70.2 ; 75.1 ; 76.4 ; 78.9 ; 83.1 ; 90.6 ; 105.8 ; 112 ; 120.9 ; 133.4 ; 134.7 ; 139.4 ; 146.7 ; 153.8 ; 160.3 ; 163.7 ; 169.6 ; 175.4 ; 177.9 ; 188 ; 188.4 ; 190.9 ; 194.3 ; 196.4 ; 202.9 ; 204.2 ; 210.8 ; 215.1 ; 216.6 ; 221.9 ; 223.3

Table 6: calculated Raman-active modes at Γ point for $Ba_{24}Ge_{100}$ from DFT.

Infrared modes	Calculated frequency modes (in cm^{-1})
T_1 symmetry	16.5 ; 18.3 ; 29.7 ; 37.7 ; 42.3 ; 46 ; 53.2 ; 53.8 ; 57.6 ; 58.4 ; 59.5 ; 60.4 ; 63 ; 64.3 ; 67.1 ; 69.5 ; 70.5 ; 74.2 ; 76.8 ; 81.3 ; 83.9 ; 88.4 ; 92.2 ; 104.9 ; 108.5 ; 113.8 ; 129.2 ; 130.8 ; 141.2 ; 144 ; 155.3 ; 158.8 ; 166.2 ; 172.7 ; 176.8 ; 185.4 ; 188.2 ; 189.5 ; 191.5 ; 195.4 ; 197.6 ; 204.5 ; 212.6 ; 214 ; 215.4 ; 221.8 ; 222.7

Table 7: calculated infrared-active modes at Γ point for $Ba_{24}Ge_{100}$ from DFT.

Silent modes	Calculated frequency modes (in cm^{-1})
A_2 symmetry	19.9 ; 21.8 ; 43.4 ; 53.9 ; 63.3 ; 64.6 ; 71.6 ; 80.4 ; 96.6 ; 119.5 ; 140.1 ; 146 ; 154.2 ; 169.3 ; 201.4 ; 209.5 ; 223

Table 8: calculated optically silent modes at Γ point for $Ba_{24}Ge_{100}$ from DFT.

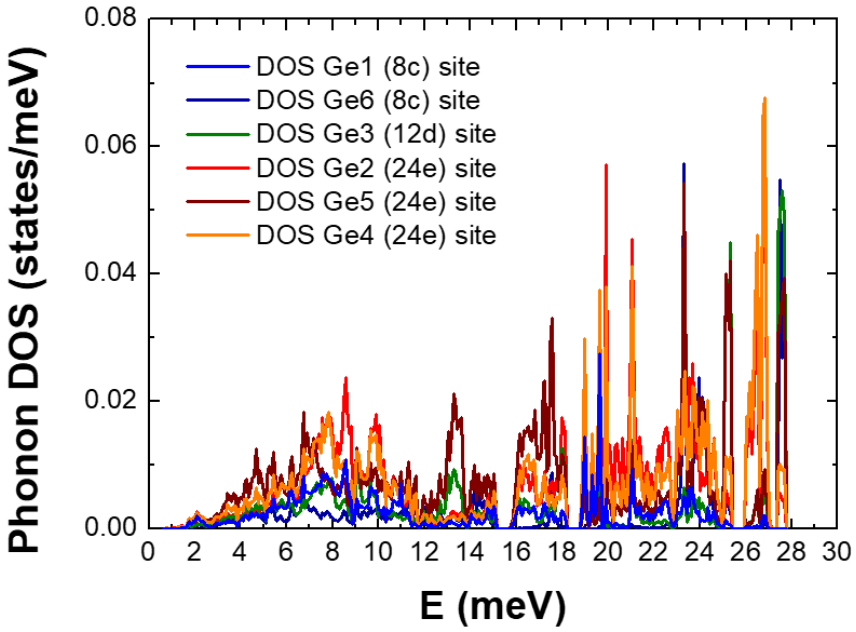

Figure 13: Atom-projected phonon density of states of the Ge atoms of $Ba_{24}Ge_{100}$ obtained from DFT calculations

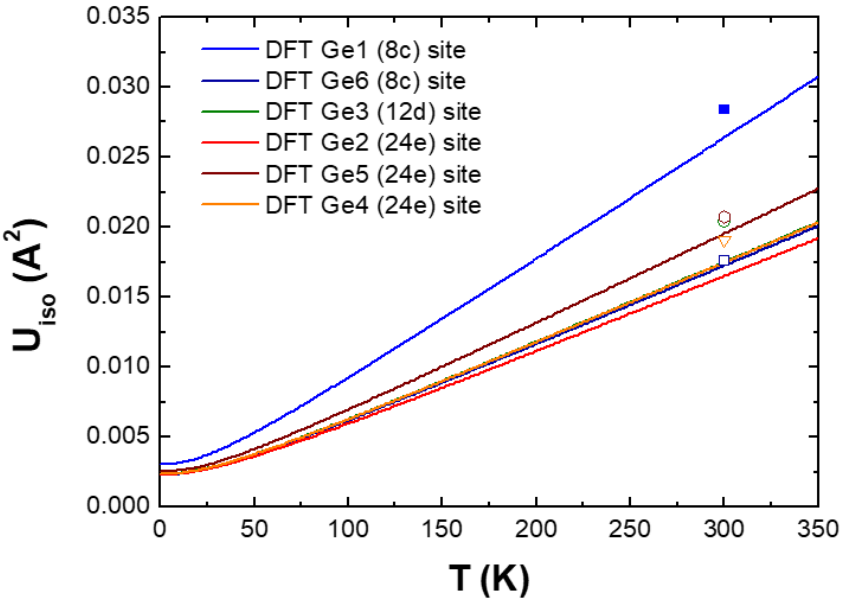

Figure 14: Isotropic atomic displacements parameters U_{iso} of germanium atoms of $Ba_{24}Ge_{100}$ from DFT calculations compared to experimental results of Fukuoka et al [13].

Appendix C: Low resolution INS results

We report the density maps recorded at IN5 with 1.8 Å incident wavelength and different temperatures in the Figure 15. We report in the Figure 16 the Q cut through the dynamic susceptibility divided by the energy for 2.3 ± 0.2 Å^{-1}, 2.8 ± 0.2 Å^{-1} and 3.5 ± 0.2 Å^{-1}, from IN5 experiments with $\lambda = 2.5$ Å. The data highlight the consistent behavior of the afore discussed low-energy excitations at higher Q numbers. Note that at the lowest T of 75 K the susceptibility at the Stokes line is obscured by the strong elastic intensity below 4 meV.

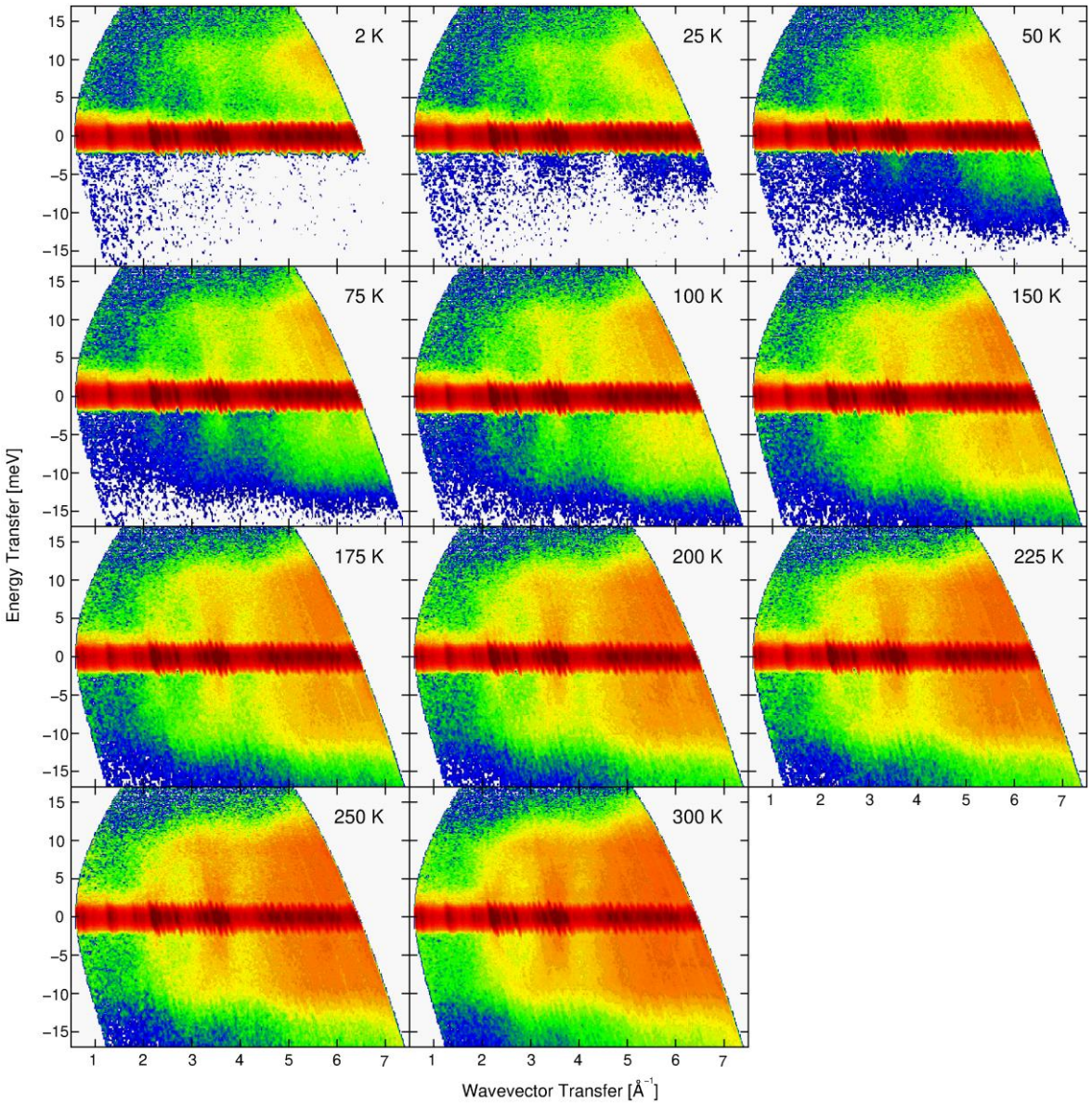

Figure 15: Intensity maps of the dynamic structure factor of $Ba_{24}Ge_{100}$ measured on IN5 with an incident wavelength of 1.8 Å at the indicated temperatures. Positive energies denote the Stokes line, negative energies the anti-Stokes line signals.

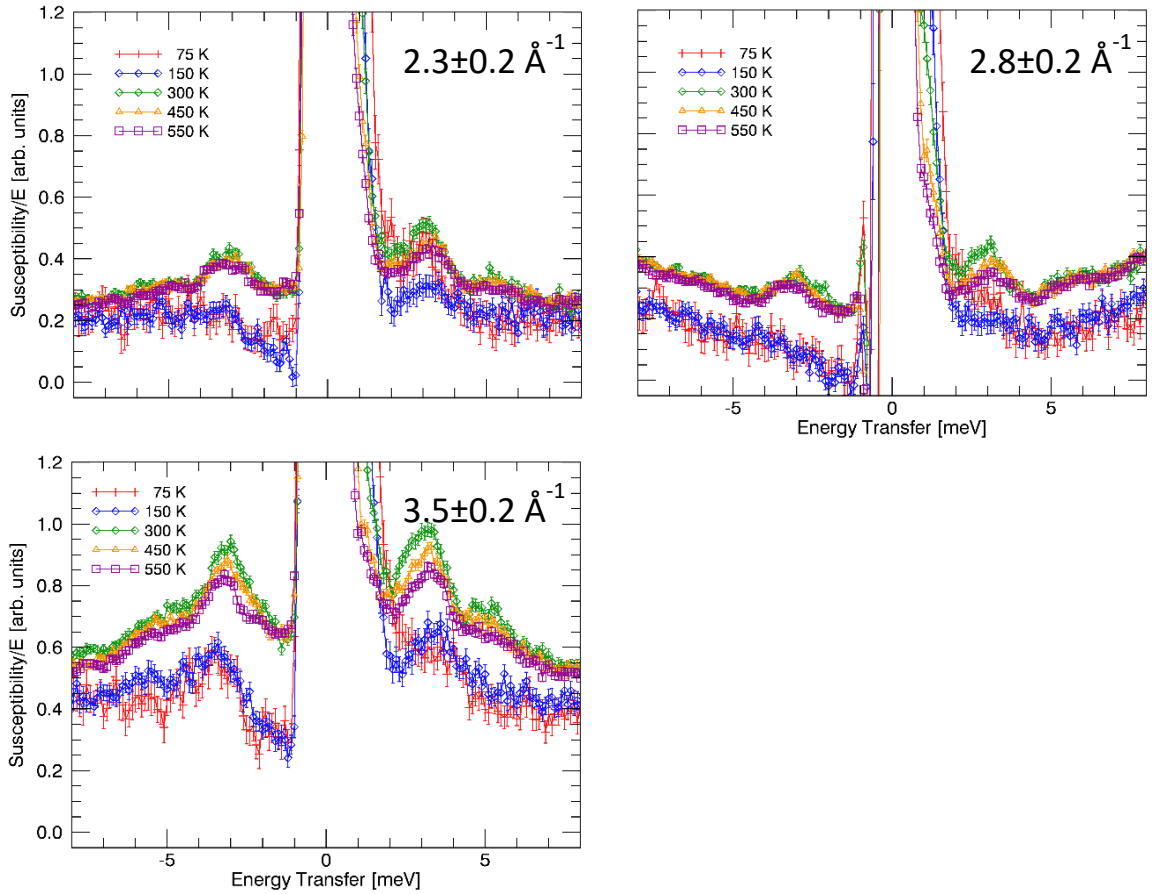

Figure 16: Q cut through the dynamic susceptibility divided by the energy for 2.3 ± 0.2 Å^{-1}, 2.8 ± 0.2 Å^{-1} and 3.5 ± 0.2 Å^{-1}, from IN5 experiments with λ = 2.5 Å. Left, anti-Stokes line and right, Stokes line. 20 K data not shown due to enhanced background.

References

[1] G. J. Snyder and E. S. Toberer, *Nat. Mat.* **7**, 105 (2008) and ref. therein

[2] G. A. Slack in *CRC Handbook of Thermoelectricity*, ch. 34 (1995)

[3] B. C. Sales, D. Mandrus, R. K. Williams, *Science* **272**, 1325 (1996)

[4] M. Christensen, S. Johnsen, B. B. Iversen, *Dalton Trans.* **39**, 978 (2010)

[5] C. H. Lee, I. Hase, H. Sugawara, H. Yoshizawa, H. Sato, *J. Phys. Soc. Jpn.* **75**, 123602 (2006)

[6] M. M. Koza, M. R. Johnson, R. Viennois, H. Mutka, L. Girard, D. Ravot, *Nat. Mater.* **7**, 805 (2008)

[7] M. M. Koza, M. Boehm, E. Sischka, W. Schnelle, H. Mutka, A. Leithe-Jasper, *Phys. Rev. B* **91**, 014305 (2015)

[8] R. Lortz, R. Viennois, A. Petrovic, Y. Wang, P. Toulemonde, C. Meingast, M. M. Koza, H. Mutka, A. Bossak, A. San Miguel, *Phys. Rev. B* **77**, 224507 (2008)

[9] H. Mutka, M. M. Koza, M. R. Johnson, Z. Hiroi, J.-I. Yamaura, Y. Nagao, *Phys. Rev. B* **78**, 104307 (2008)

[10] M. M. Koza, H. Mutka, Y. Okamoto, J.-I. Yamaura, Z. Hiroi, *Phys. Chem. Chem. Phys.* **17**, 24837 (2015)

[11] T. Takabatake, K. Suekuni, T. Nakayama, E. Kaneshita, *Rev. Mod. Phys.* **86**,669 (2014)

[12] R. Viennois, M. M. Koza, R. Debord, P. Toulemonde, H. Mutka, S. Pailhès, *Phys. Rev. B* **101**, 224302 (2020)

[13] H. Fukuoka, K. Iwai, S. Yamanaka, H. Abe, K. Yoza, L. Häming, *J. Solid State Chem.* **151**, 117 (2000)

[14] S.-J. Kim, S. Hu, C. Uher, T. Hogan, B. Huang, J. D. Corbett, M. G. Kanatzidis, *J. Solid State Chem.* **153**, 121 (2000)

[15] W. Carrillo-Cabrera, J. Curda, H. G. von Schnering, S. Paschen, Y. Grin, *Z. Kristallogr. NCS* **215**, 207 (2000)

[16] F. M. Grosche, H. Q. Yuan, W. Carrillo-Cabrera, S. Paschen, C. Langhammer, F. Kromer, G. Sparn, M. Baenitz, Y. Grin, F. Steglich, *Phys. Rev. Lett.* **87**, 247003 (2001)

[17] S. Paschen, V. H. Tran, M. Baenitz, W. Carrillo-Cabrera, Y. Grin, F. Steglich, *Phys. Rev. B* **65**, 134435 (2002)

[18] V. Petkov, T. Vogt, *Solid State Commun.* **127**, 43 (2003)

[19] M. Schmidt, P. G. Radaelli, M. J. Gutmann, S. J. L. Billinge, N. Hur, S. W. Cheong, *J. Phys.: Cond. Matter.* **16**, 7287 (2004)

[20] W. Carrillo-Cabrera, H. Borrmann, S.Paschen, M. Baenitz, F. Steglich, Y. Grin, *J. Solid State Chem.* **178**, 715 (2005)

[21] I. Zerec, A. Yaresko, P. Thalmeier, Y. Grin, *Phys. Rev. B* **66**, 045115 (2002)

[22] I. Zerec, W. Carrillo-Cabrera, V. Voevodin, J. Sichelschmidt, F. Steglich, Y. Grin, A. Yaresko, S.-I. Kimura, *Phys. Rev. B* **72**, 045122 (2005)

[23] T. Rachi, M. Kitajima, K. Kobayashi, F. Guo, T. Nakano, Y. Ikemoto, K. Kobayashi, K. Tanigaki, *J. Chem. Phys.* **123**, 074503 (2005)

[24] J. Tang, J. Xu, S. Heguri, H. Fukuoka, S. Yamanaka, K. Akai, K. Tanigaki, *Phys. Rev. Lett.* **105**, 176402 (2010)

[25] F. Kanetake, A. Harada, T.Rachi, H. Nagara, H. Mukuda, K. Kusakabe, Y. Kitaoka, N. Suzuki, K. Tanigaki, K. Itoh, E. E.Haller, *J. Phys. : Conf. Ser.* **121**, 052011 (2008)

[26] F. Kanetake, A. Harada, H. Mukuda, Y. Kitaoka, T.Rachi, K. Tanigaki, K. Itoh, E. E.Haller, *J. Phys. Soc. Jpn.* **78**, 104710 (2009)

[27] H. Q. Yuan, F. M. Grosche, W. Carrillo-Cabrera, V. Pacheco, G. Sparn, M. Baenitz, U. Schwarz, Y. Grin, F. Steglich, *Phys. Rev. B* **70**, 174512 (2004)

[28] J.-H. Kim, N. L. Okamoto, K. Kishida, K. Tanaka, H. Inui, *Acta Mater.* **54**, 2057 (2006)

[29] J.-H. Kim, N. L. Okamoto, K. Kishida, K. Tanaka, H. Inui, *J. Appl. Phys.* **102**, 034510 (2007)

[30] J.-H. Kim, N. L. Okamoto, K. Kishida, K. Tanaka, H. Inui, *J. Appl. Phys.* **102**, 094506 (2007)

[31] H. Shimizu, T. Fukushima, T. Kume, S. Sasaki, H. Fukuoka, S. Yamanaka, *J. Appl. Phys.* **101**, 113531 (2007)

[32] J. Rodriguez-Carvajal, *Applied Crystal.*30 (2001)

[33] M. M. Koza, A. Leithe-Jasper, H. Rosner, W. Schnelle, H. Mutka, M. R. Johnson, Y. Grin, *Phys. Rev. B* **89**, 014302 (2014)

[34] M. M. Koza, M. R. Johnson, H. Mutka, M. Rotter, N. Nasir, A. Grytsiv, P. Rogl, *Phys. Rev. B* **82**, 214301 (2010)

[35] M. M. Bredov, B. A. Kotov, N. M. Okuneva, V. S. Oskotskii, A. L. Shakh-Budagov, *Sov. Phys. Solid State* **9**, 214 (1967)

[36] V. S. Oskotskii, *Sov. Phys. Solid State* **9**, 420 (1967)

[37] G. Kresse, D. Joubert, *Phys. Rev. B* **59,** 1758 (1999)

[38] J. P. Perdew, K. Burke, M. Ernzerhof, *Phys. Rev. Lett.* **77**, 3865 (1996)

[39] M. Methfessel, A. T. Paxton, *Phys. Rev. B* **40,** 3616 (1989)

[40] H. J. Monkhorst, J. D. Pack, *Phys. Rev. B* **13,** 5188 (1976)

[41] J. Hafner, *J. Comput. Chem.* **29**, 2044 (2008)

[42] P. Vinet, J.-H. Rose, J. Ferrante, J.-R. Smith, *J. Phys.: Condens. Matter* **1**, 1941 (1989)

[43] K. Parlinski, Z.-Q. Li, Y. Kawazoe, *Phys. Rev. Lett.* **78**, 4063 (1997)

[44] M. M. Koza, L. Capogna, A. Leithe-Jasper, H. Rosner, W. Schnelle, H. Mutka, M. R. Johnson, C. Ritter, Y. Grin, *Phys. Rev. B* **81**, 174302 (2010)

[45] H. Euchner, S. Pailhès, L. T. K. Nguyen, W. Assmus, F. Ritter, A. Haghighirad, Y. Grin, S. Paschen, and M. de Boissieu, *Phys. Rev. B* **86**, 224303 (2012)

[46] S. Pailhès, H. Euchner, V. M. Giordano, R. Debord, A. Assy, S. Gomes, A. Bosak, D. Machon, S. Paschen, M. de Boissieu., *Phys. Rev. Lett.* **113**, 025506 (2014)

[47] C. Candolfi, U. Aydemir, M. M. Koza, M. Baitinger, Yu. Grin, F. Steglich, *J. Phys.: Cond. Mat.* **27**, 485401 (2015)

[48] H. Euchner, A. Groß, *Chem. Mater*. **31**, 2571 (2019)

[49] P.-F. Lory *et al.*, *Nat. Commun.* **8**, 491 (2017)

[50] M. Christensen, A. B. Abrahamsen, N. B. Christensen, F. Juranyi, N. H. Andersen, K. Lefmann, J. Andreasson, C. R. H. Bahl, B. B. Iversen, *Nat. Mater.* **7**, 811 (2008)

[51] N. Melnychenko-Koblyuk *et al.*, *J. Phys.: Condens. Matter* 19, 216223 (2007)

[52] N. Melnychenko-Koblyuk *et al.*, *Phys. Rev. B* 76, 144118 (2007)

[53] N. L. Okamoto, J.-H. Kim, K. Tanaka, H. Inui, *Acta Mater.* **54**, 5519 (2006)

[54] H. Fukuoka and S. Yamanaka, *J. Organomet. Chem.* **611**, 543 (2000)

[55] T. F. Fässler, C. Kronseder, *Z. Anorg. Allg. Chem.* **624**, 561 (1998)

[56] H. G. von Schnering, A. Zürn, J.-H. Chang, M. Baitinger, Y. Grin, *Z. Anorg. Allg. Chem.* **633**, 1147 (2007)

[57] T. Dahm, K. Ueda, *Phys. Rev. Lett.* **99**, 187003 (2007)

[58] G. Lucazeau, *J. Raman Spectrosc.* **34**, 478 (2003)

[59] G. A. Kourouklis, E. Anastassakis, *Phys. Stat. Sol. (b)* **152**, 89 (1989)

[60] M. Falmbigl, G. Rogl, P. Rogl, M. Kriegish, H. Müller, E. Bauer, M. Reinecker, W. Schranz, *J. Appl. Phys.* **108**, 043529 (2010)

[61] P. Toulemonde, D. Machon, A. San Miguel, M. Amboage, *Phys. Rev. B* **83**, 134110 (2011)

[62] A. San Miguel, P. Mélinon, D. Connétable, X. Blase, F. Tournus, E. Reny, S. Yamanaka, J. P. Itié, *Phys. Rev. B* **65**, 054109 (2002)